Geophysical Research Letters

Key Points:
- Spectral ratio method is applied to resolve source parameters of microearthquakes activated during a fluid injection experiment
- Microearthquakes rupture multiple meter-scale source patches in a network of preexisting fractures
- Relative stress drops of experimental microearthquakes fall in the low end of those of induced earthquakes in the central United States

Correspondence to:
Y. Huang,
yiheh@umich.edu

Illuminating the Rupturing of Microseismic Sources in an Injection-Induced Earthquake Experiment

Yihe Huang[1] , **Louis De Barros[2]** , **and Frédéric Cappa[2,3]**

[1]Department of Earth and Environmental Sciences, University of Michigan, Ann Arbor, MI, USA, [2]Université Côte d'Azur, CNRS, Observatoire de la Côte d'Azur, IRD, Géoazur, Sophia Antipolis, France, [3]Institut Universitaire de France, Paris, France

Abstract We analyze source parameters of M_w −3.9 to −3.1 induced earthquakes during an in situ fluid injection experiment in France using the spectral ratio method based on empirical Green's function. We choose 10 event pairs with highly similar waveforms and resolve their spectral ratios using multiple S wave windows. We find that master events ruptured meter-scale source patches with <1-μm slip in a preexisting fracture network oriented differently from the injected plane. The temporal correlation between master earthquake occurrence and injection pressure peak and the relatively low ratio of stress drop to crustal strength suggest that both fluid pressure perturbation and aseismic deformation play important roles in inducing the earthquakes. The comparison between stress drops of induced earthquakes in the experiment and in the central United States indicates a dependency of stress drop on crustal shear strength.

Plain language summary Numerous small and moderate injection-induced earthquakes have been recorded in North America, Europe, and Asia. Here we present a detailed analysis about microearthquakes in an in situ injection-induced earthquake experiment, which provides an unprecedented opportunity to investigate the mechanisms of induced earthquakes. Our analysis illuminates meter-scale earthquake sources distributed in a network of preexisting rock fractures. The majority of induced earthquakes in our analysis happened when injection pressure reached a peak, indicating a direct response of rock fractures to fluid pressure perturbation. But the relatively low ratio of stress drop to crustal strength reveals that a very small fraction of the crustal shear strength is released by earthquakes, supporting the previous notion that fluid injection induces large aseismic deformation during the experiment.

1. Introduction

It is well known that fluid injection can induce earthquakes (Ellsworth, 2013; Keranen & Weingarten, 2018), but how fluid induces earthquakes initially and then contributes to the sequences of earthquakes following afterward is still puzzling. Fluid pressure is usually considered as the major driving force in the generation of induced earthquakes when injection wells are close to the fault (Raleigh et al., 1976), whereas stress loading due to poroelastic deformation can take over when injection wells are more distant (Goebel & Brodsky, 2018; Segall & Lu, 2015). Geomechanical models show that the current injection wells in Oklahoma (USA) can induce fluid pressure and stress loading of the order of 0.1 MPa (Keranen et al., 2014), which is much smaller than the stress drop estimates of moderate-magnitude-induced earthquakes that have a median stress drop of about 1–20 MPa (Boyd et al., 2017; Huang et al., 2017; Trugman et al., 2017; Wu et al., 2018). The small ratio of fluid pressure perturbation and earthquake stress drop suggests that faults are almost critical before injection takes place (Townend & Zoback, 2000) and even a small fluid pressure or stress perturbation can make the faults reach favorable conditions for earthquake nucleation. The following earthquake sequences not only rely on the stress budget accumulated in the tectonic history but also involve stress perturbations transferred by the cascading failure (Catalli et al., 2016; Schoenball & Ellsworth, 2017; Sumy et al., 2014) and carried by aseismic slip (Bhattacharya & Viesca, 2019; Cappa et al., 2019; Guglielmi et al., 2015; Wei et al., 2015).

A deeper understanding of the mechanisms of induced seismicity sequences requires a higher-resolution observation of the spatial-temporal evolution of earthquake source patches. The cascades of earthquakes can manifest themselves as contiguous source patches, whereas earthquakes driven by aseismic slip may repeat rupturing the same source patches (Ellsworth & Bulut, 2018; Gomberg, 2018). For induced
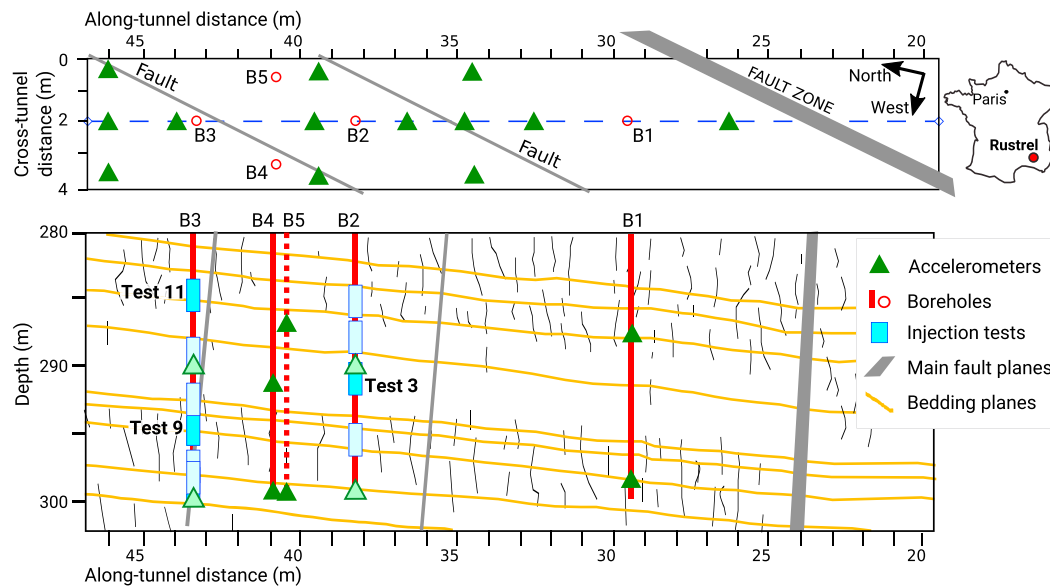
Figure 1. Horizontal (top) and vertical (bottom) views of the experiment. The main fault (gray thick line), secondary faults (gray thin lines), the location for the vertical view (blue dashed line), bedding planes (yellow lines), boreholes (red circles and lines), injection intervals (blue rectangles), and accelerometers (green triangles) are represented.

seismicity sequences, the injection pressure data can be used to estimate the contribution of fluid pressure (Walsh & Zoback, 2015). Comparing the spatial-temporal evolution of earthquake sequence with the injection pressure may lead to more details about the mechanical response of faults to fluid injection. However, injection data are usually available in the monthly or daily scale, and few can reach the precision needed for interpreting its relationship with earthquakes that occur within seconds.

To provide insights into the interplay of the evolution of fluid injection and earthquake rupture, we analyze earthquake source parameters in an injection experiment at 280-m depth within the Low Noise Underground Laboratory facility (http://lsbb.eu) in France (Guglielmi et al., 2015). A series of 11 injection tests were performed to reactivate selected geological features belonging to the damaged zone (20 m thick) of a kilometer-long inactive fault (Figure 1). A borehole probe, called the step-rate injection method for fracture in situ properties probe (Guglielmi et al., 2014), was used to inject water into 2.4-m-long sections isolated between packers in vertical boreholes. At the injection point, this probe was also used to monitor the fluid pressure, the flowrate, and the deformation through optical fiber sensors. To monitor seismicity, 14 vertical and 8 three-component accelerometers were set on the gallery floor and on adjacent boreholes, respectively, at distances of 3–20 m from the injection. These 10-Hz to 4-kHz sensors allow the analysis of the seismicity in a broad frequency range. For more details about this experiment, we refer the reader to Duboeuf et al. (2017) and De Barros et al. (2018). Our results mainly come from Injection Test 11 during which the largest number of earthquakes (110 events above magnitude −4.1) occurred. The probe was centered at a depth of 4.4 m below the tunnel floor on a set of bedding planes (dip direction, N120; dip angle, 20–30°) that separate layers of low-porosity (ϕ = 2–5%; Jeanne et al., 2012) limestone intersected by subvertical fractures during the test. Data from two other tests ("3.a" and "9") are also used. These injections, at 9.4 and 13.9 m below the gallery floor, reactivated a subvertical fracture and a bedding plane and induced 38 and 18 seismic events above magnitude −4.2, respectively.

Here we apply a spectral ratio approach to estimate the source dimension and stress drop of these induced events. Duboeuf et al. (2017) have analyzed their corner frequencies by assuming a constant attenuation model for the propagation paths. The spectral ratio method used here can more effectively remove the propagation and site effects, which may lead to higher stress drops than the constant attenuation approach (Ide et al., 2003). The new approach also enables us to quantify the uncertainties of source parameters. We reveal unprecedented details of earthquake rupture patterns in response to injection and compare their source parameters to those of induced earthquakes in the central United States.

## 2. Spectral Ratio Analysis of Microseismic Sources

We use seismic data recorded by the vertical component of the 22 sensors at a rate of 10,000 samples per second to carry out a spectral ratio analysis of events with highly similar waveforms (Abercrombie, 2015; Huang et al., 2016). We first cross-correlate waveforms of previously detected earthquakes, including both P and S waves filtered between 200 and 2,000 Hz, and identify pairs of earthquakes that have cross-correlation coefficients higher than 0.8 at more than three stations (Figures 2a–2c). Most highly similar earthquake pairs occurred during the first 1.6 hr of Injection Test 11. Abercrombie (2015) showed that lower cross-correlation coefficients will lead to larger variability of spectral ratios and a decrease in corner frequency estimates. We refer the earthquake with the largest source dimension (i.e., lower corner frequency) in the cluster as the master earthquake and the remaining as the empirical Green's functions (eGfs). Assuming the Brune source model (Brune, 1970), we can describe the spectral ratio of the master earthquake and its eGf as

$$\frac{u_1(f)}{u_2(f)} = \frac{M_{01}}{M_{02}} \left(\frac{1 + \left(\frac{f}{f_{c2}}\right)^2}{1 + \left(\frac{f}{f_{c1}}\right)^2} \right), \tag{1}$$

where $u_1(f)$ is the acceleration spectrum of the master event and $u_2(f)$ is the acceleration spectrum of the eGf. There are three unknowns in the spectral ratio, including the moment ratio M_{01}/M_{02}, corner frequency of the master event f_{c1}, and of the eGf f_{c2}. The moment ratio and corner frequency of the master event are better resolved than the corner frequency of the eGf, as the spectral ratio plateau at high frequencies is absent in our data due to the limited bandwidth. The moment ratio is usually observed to be higher than 1, as earthquakes with larger source dimension often have higher magnitudes. However, our analysis reveals that master earthquakes may have lower magnitudes but larger source dimensions than eGfs (Figure 2h), indicating that master earthquakes can release smaller slip than their eGfs.

We acknowledge the sensitivity of spectral ratios to noise levels when the moment ratio is small. To reduce the uncertainty of the spectral ratio analysis, we use various numbers of S wave windows with different durations of 0.002–0.005 s overlapped by half the window duration to calculate the spectrum and sample the spectrum between 100-300 Hz and 2,500-4,000 Hz at equal intervals in log frequency. We focus on the S waves as the P wave window is too short to obtain stable spectral ratio results. We find the best fit spectral ratio to the Brune source model (Imanishi & Ellsworth, 2006), that is, smallest misfit between the observed spectral ratio and the modeled spectral ratio, using the trust-region-reflective-optimization approach (Huang et al., 2017). This approach minimizes a function $f(x)$ by approximating it using a simpler function q around the point x in a neighborhood N (Moré & Sorensen, 1983).

We also estimate the uncertainty by bootstrapping the misfit between the observed and best fit spectral ratios. We construct 1,000 synthetic spectral ratios for each master-eGf pair by adding the bootstrapping misfit at each frequency to the best fit spectral ratio and obtain distributions of moment ratios and corner frequencies (Figures 2d and 2e). We show that a well-constrained spectral ratio should lead to Gaussian-like distributions of moment ratios and corner frequencies of master events that are within the resolvable frequency band of the data (Figure 2e). We use 95% confidence interval of corner frequency estimates in the bootstrapping analysis to estimate the possible range of source radius. Note that the uncertainty from the bootstrapping analysis is primarily the measurement uncertainty, which is likely smaller than the real uncertainty caused by the unknown source geometry and rupture process. The spectral ratio method leads to well-constrained results for less than a third of the master-eGf pairs identified from the highly similar waveforms (Figures 2f–2h and S1). It is likely that the remaining earthquakes either have higher corner frequencies than the maximum usable frequency of the data (4000 Hz), which is 80% of the Nyquist frequency, or more complicated source processes (Denolle & Shearer, 2016; Uchide & Imanishi, 2016). The eGf corner frequencies are more difficult to resolve due to the limited bandwidth of the records. However, since the eGfs and master event have highly similar waveforms in the 200- to 2,000-Hz frequency band, the corner frequencies of the eGfs are likely to be higher than 2,000 Hz, which is assumed as a lower bound for the eGf corner frequencies and used to estimate the higher bound of their source dimensions (Figure 3).
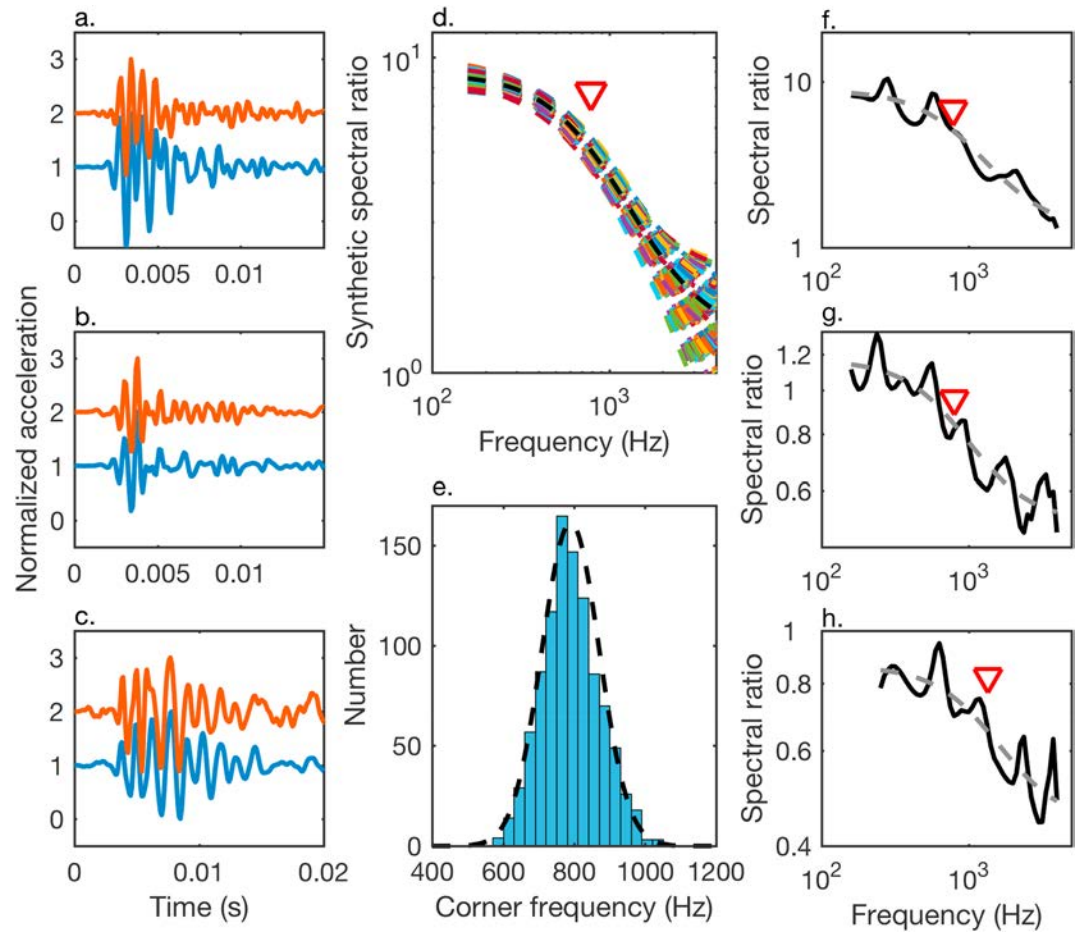
Figure 2. (a–c) Highly similar waveforms of one master event (blue) and its empirical Green's function (red) recorded by three stations. (d and e) 1,000 synthetic spectral ratios in the bootstrapping analysis and the distribution of resulting corner frequencies. The black dashed line gives the Gaussian distribution with the mean and standard deviation of the resolvable corner frequencies. (f–h) Observed (solid line) and modeled (dashed line) S wave spectral ratios. Red triangles denote master event corner frequencies.

3. Spatial-Temporal Evolution of Earthquake Source Patches

We estimate corner frequencies of 10 pairs of highly similar events (eight master earthquakes) that have Brune-type spectral ratios (Figure S1). The new corner frequencies are comparable to the values obtained by Duboeuf et al. (2017). The largest difference between the estimates for a certain event is about a factor of 2 (Table S1). To calculate the source dimension from corner frequency estimates (Figures 3 and 4a), we assume a circular crack model (Eshelby, 1957) and an S wave velocity (v_s) of 2,750 m/s (Duboeuf et al., 2017):

$$r = \frac{kv_s}{f_c},$$ (2)

where r is the source radius. Assuming a rupture velocity that is 90% of the S wave velocity, we use $k = 0.26$ for symmetric circular rupture obtained by Kaneko and Shearer (2015), who solve the issue of singular stress at the rupture front that exists in the Madariaga's model (Madariaga, 1976). The k parameter for symmetric circular rupture in Kaneko and Shearer (2015) is constantly 0.26 for rupture velocities between 70% and 90% and drops slightly to 0.25 for a rupture velocity of 60%. It also lies between the Brune ($k = 0.372$; Brune, 1970) and Maradiaga source parameters ($k = 0.21$) that can lead to a factor of 1.77 difference in rupture radius estimation. The estimated rupture radius ranges between 0.39 and 0.89 m (Figure 4a). The Brune source parameter results in larger rupture patches and overlap of events, whereas the Madariaga source parameter leads to the lower bound of rupture dimensions (Figures S2 and S3).
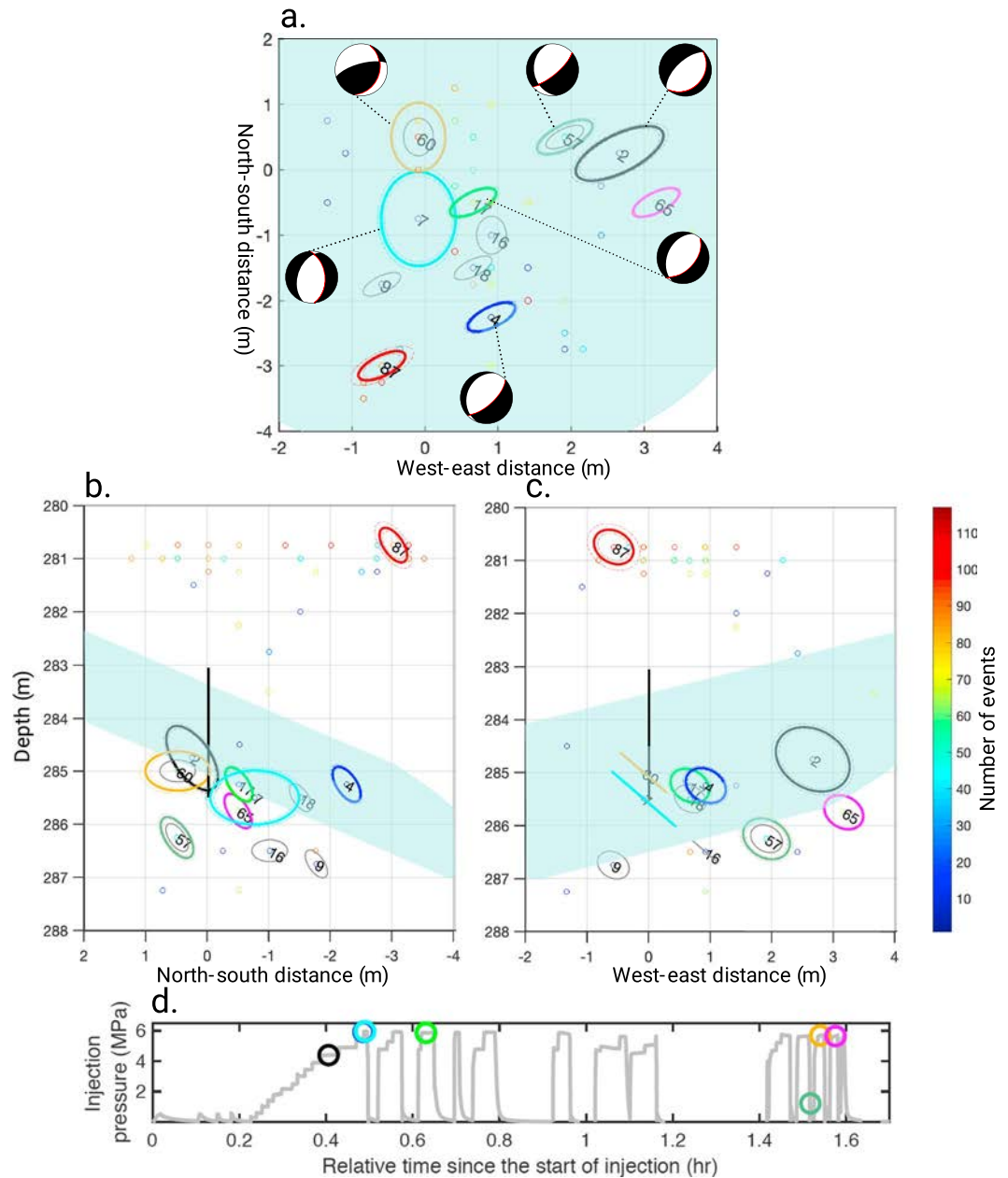
Figure 3. (a–c) Distribution of rupture patches of master events (large colored circles) and empirical Green's function events (large gray circles) and (d) correlation between master events and injection pressure during Test 11. The focal mechanisms of master events are shown in (a). The black bar and light blue plane indicate the injection borehole and injected bedding plane, respectively. Master Events 2, 4, 7, 17, 57, 60, 65, and 87 are indicated by black, blue, cyan, green, olive, yellow, magenta, and red circles with thick lines. Circles with thin lines show the possible range of source patches obtained from bootstrapping. Small colored circles represent earthquakes whose locations can be resolved. Their order of occurrence is represented by the color bar. In (d), blue and cyan circles are almost overlapped, and the red circle is not shown since Event 87 happened ~3.3 hr after Event 2.

The magnitudes were computed by Duboeuf et al. (2017) by fitting a Brune's model in acceleration, following Boore (1983). They used a quality factor $Q = 50$ for the attenuation to obtain a flat plateau at high frequency and averaged the results from all sensors and components to remove radiation pattern effects (Daniel, 2014). The inferred magnitudes lie between M ~ −3.1 and −4.0. We benchmark the moment magnitudes of master events using moment ratios of the master and eGf events calculated from the spectral ratio method since several master events share the same eGf events. For the master events that do not share eGfs with the others,
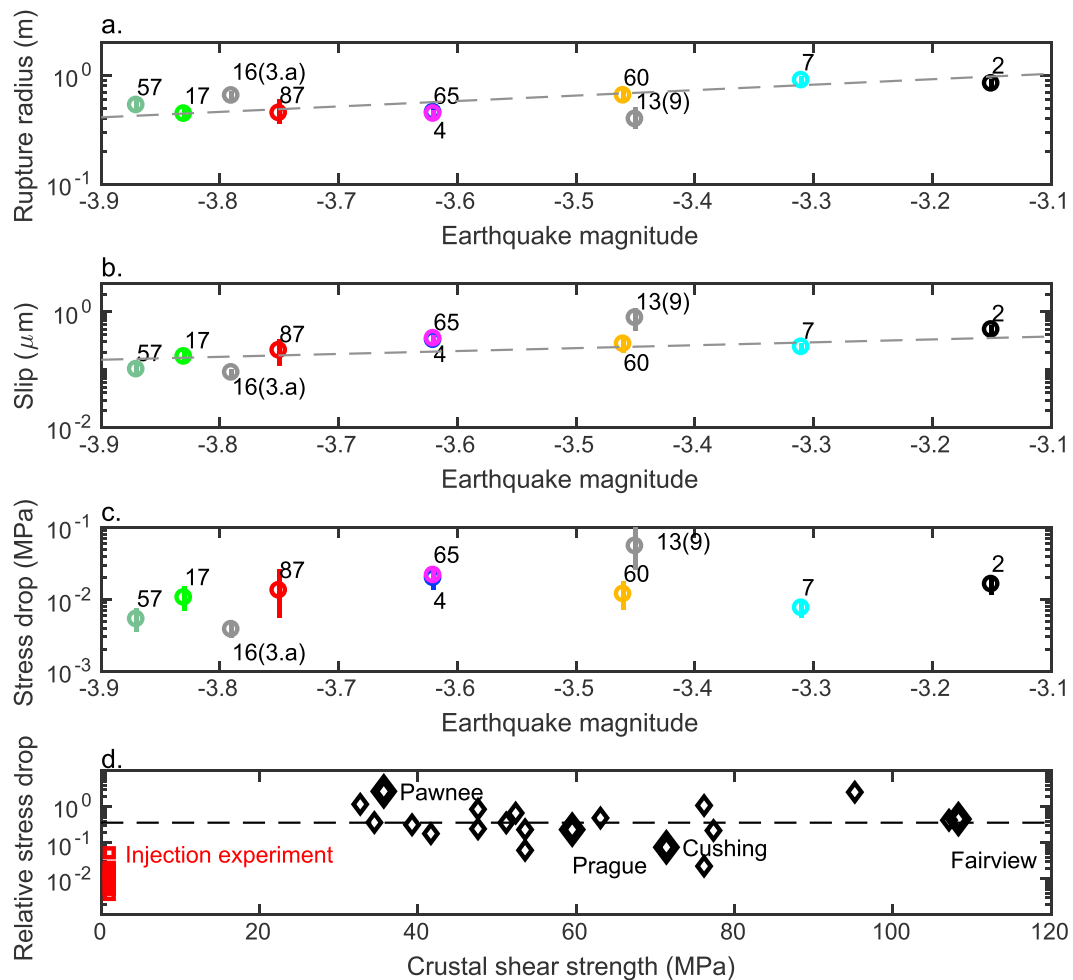
Figure 4. (a–c) Rupture radius, slip, and stress drop estimates of master events are shown with error bars indicating 95% confidence level of corner frequencies. Event 16 from Injection Test 3.a and Event 13 from Injection Test 9 are shown by gray circles. The gray dashed lines in (a) and (b) demonstrate the predicted relationships from a circular crack model with 0.01-MPa stress drop. (d) Relative stress drops of M_w −3.9 to −3.1 master events in the experiment (red) and of M_w 3.3 to 5.7 induced earthquakes in the central United States (black) analyzed in Huang et al. (2017). Larger diamonds denote $M_w \geq 5$ earthquakes in Prague, Fairview, Cushing, and Pawnee in Oklahoma. The black dashed line shows the median relative stress drop of induced earthquakes in the central United States.

we assume the larger magnitudes are better resolved and correct the other event in the pair using the moment ratio.

We compute double-couple mechanisms by a grid search approach (HASH software; Hardebeck & Shearer, 2002) after manually picking the polarity of the first arrivals. As master events and their eGfs should share a similar location and mechanism, we derive composite mechanisms for pairs of events (Figures 3a and S4). From the borehole logs and plugs, the orientation of the main fractures and the bedding planes are determined (Duboeuf et al., 2017) and correlated with the inferred focal planes. Interestingly, while the main structures that cross the injection interval are bedding planes with a low dip angle (20–30°), no focal planes with such orientations are observed. As water leakages were observed where these planes reach the tunnel floor, they are the main pressurized planes, but they are not slipping seismically. On the contrary, computed nodal planes are compatible with fractures with a high dip angle (Figure 3).

We name the events based on the chronological order of occurrence during the injection test. These events and their eGfs also represent 75% of microearthquakes, whose locations can be resolved, occurring at depths of 284–287 m for the first 1.6 hr of the test. Our results show that the Master Earthquakes 2, 4, 7, 17, 57, 60, 65, and 87 ruptured multiple meter-scale source patches that may lie on different fracture planes (Figure 3). But given the earthquake location uncertainty of ~1 m (Duboeuf et al., 2017), some earthquakes may have ruptured and reruptured the same fracture. The proximity and similar focal mechanisms of Events 7 and

60 suggest that they are colocated on the same fracture plane, oriented N0°E to 45°E. Events 2, 4, 17, 57, and 65 are also likely to rupture the same structure oriented N60°E to 65°E. Both sets of fracture planes are nearly orthogonal to the bedding plane in which fluid pressure is injected. Therefore, the deformation on the injected plane appears mostly aseismic and efficiently triggers seismicity on branching subvertical fractures that surround it.

Comparing the temporal evolution of these master earthquakes with the pressure data shows that fractures can quickly respond to pressure perturbation by releasing stresses during earthquakes after the fault is prepared for slip by pressure build-up and aseismic deformation (Figure 3d). Five out of eight master events occurred at the peak of injection pressure (~6 MPa), indicating the meter-scale fault slips at a critical pressure level acting on the ruptured region. In the first stage of Injection Test 11, Events 2 and 4 broke a fracture nearly orthogonal to the injection plane. Eleven seconds after, Event 7 ruptured another fracture when injection pressure reached almost 6 MPa. Given their close temporal proximity and nearly adjacent source patches when the location uncertainty is considered, it is possible that Event 4 indirectly triggered Event 7 through stress perturbations. Subsequent Events 17 and 57 occurred on fracture planes with the same orientation as Events 2 and 4, whereas Event 60 shared the same fracture orientation as Event 7. It seems that two sets of fractures expressed seismicity in response to pressure perturbation and aseismic motion of the injected bedding plane. Events alternated between these fractures, as if rupture on one fracture might unlock the aseismic motion and increase stress on the remaining ones.

4. Slip and Stress Drop Estimation

We estimate slip d and stress drop $\Delta\tau$ of the master earthquake from its source radius r, moment M_0, and shear modulus μ:

$$d = \frac{M_0}{\pi \mu r^2}, \tag{3}$$

$$\Delta\tau = \frac{7}{16} \frac{M_0}{r^3}. \tag{4}$$

The shear modulus is calculated from an S wave velocity of 2,750 m/s and a density of 2,670 kg/m^3.

We find that both slip and stress drops of master earthquakes during Injection Test 11 lie in a narrow range, 0.10–0.48 μm and 0.005–0.021 MPa, respectively (Figures 4b and 4c). The scaling relationship of rupture radius and slip with earthquake magnitude is consistent with the trend predicted by a constant stress drop of 0.01 MPa. The largest and smallest slip (0.77 and 0.09 μm) and stress drop estimates (0.054 and 0.004 MPa) come from two master events during Injection Tests 3.a and 9, which may be caused by the less well calibrated magnitudes compared to events during Injection Test 11. But since Injection Tests 3.a and 9 represent two separate injection intervals at different locations, the contrast of slip or stress drop estimates may reflect different fault stress, geometrical, and hydromechanical conditions. Given source radius is estimated using $k = 0.26$ that lies between the Brune and Madariaga k values, our stress drop estimates are about 1.9 times smaller than the Maradiaga estimates and 2.9 larger than the Brune estimates (Figure S5).

5. Comparison of the Relative Stress Drops of Earthquakes in the Experiment and Central United States

Our stress drop estimates of master earthquakes in the experiment are much lower than those of moderate-magnitude induced earthquakes associated with large-volume injections in the central United States (Huang et al., 2017). This comparison between two groups of earthquakes is facilitated by the same spectral ratio approach and the same assumption of a circular fault model and Brune source spectra. We also reestimate stress drops of central U.S. earthquakes using the same k parameter given by Kaneko and Shearer (2015). Since the shear modulus used in the stress drop calculation of central U.S. earthquakes is 1.44 times of the shear modulus used here, the stress drop difference cannot be explained by the difference in shear moduli. One primary factor that can cause the discrepancy is the different fault stress conditions. The principal fault stresses are in the order of 3 to 6 MPa in the experiment, whereas the fault stresses are usually in the order of hundreds of megapascals at the depths (i.e., 3–10 km) of moderate-magnitude induced

earthquakes. To compare induced earthquakes at various depths and fault conditions, we define the ratio of the stress drop to crustal shear strength as the "relative stress drop." Crustal shear strengths for reverse-faulting and normal-faulting earthquakes can be estimated from the ratio of the maximum to the minimum effective stress on optimally oriented faults (Moos & Zoback, 1990) and a friction coefficient of 0.6 (Byerlee, 1978), a typical value for crustal faults. Since earthquakes in the experiment are primarily normal-faulting earthquakes, we can estimate their crustal shear strength S_{normal} (Huang et al., 2017):

$$S_{\mathrm{normal}} = 0.34(\sigma_v - P), \tag{5}$$

where σ_v is the vertical stress and P is the fluid pressure. Here we assume the effective vertical stress $\sigma_v - P$ is 3 MPa, that is, the lower bound of principal fault stresses in the experiment. The crustal strength of induced earthquakes in the central United States that occur on strike-slip faults is assumed to be the average of the crustal shear strengths for reverse-faulting ($S_{\mathrm{reverse}} = 1.06(\sigma_v - P)$) and normal-faulting earthquakes:

$$S_{ss} = 0.7(\sigma_v - P) \tag{6}$$

We compute the effective vertical stress for central U.S. earthquakes using their depths and a gradient of 17 MPa/km (Huang et al., 2017). For four $M_w \geq 5$ induced earthquakes in Oklahoma, the Pawnee mainshock has an exceptionally high relative stress drop. The median relative stress drop of induced earthquakes in the central United States is about 0.36 (Figure 4d). The relative stress drop of master events in the experiment ranges between ~0.004 and 0.05, which falls in the low end of the relative stress drop of induced earthquakes in the central United States (~0.02–2.72). Despite large differences in depths and tectonic context, these comparable values of relative stress drop indicate a dependency of the stress drop on the shear strength. The low values of relative stress drop of earthquakes in the experiment also indicate that a very small fraction of the crustal shear strength has been released seismically. This is consistent with the previous finding that fluid injection induces substantial aseismic deformation (Guglielmi et al., 2015), as less than 1e−4% of the injection energy induces deformation, whose aseismic component is more than 99% (De Barros et al., 2019).

6. Conclusion

Here we use the spectral ratio method based on eGfs to estimate the source parameters of M_w −3.9 to −3.1 induced earthquakes observed during a fluid injection experiment at 280-m depth. We find that meter-scale microearthquake sources are distributed in a network of preexisting fractures surrounding the main plane where the fluid is injected and slip is aseismic. Sequences of microearthquakes are triggered when injection pressure is high and sufficient aseismic deformation is developed in the injected plane. Stress drop values have a narrow range and constitute a small fraction of crustal shear strength, consistent with the previous notion that fluid injection induces large aseismic deformation during this experiment. We also find that the relative stress drops of microearthquakes in the experiment fall in the low end of those of central U.S. induced earthquakes. Their variations imply a sensitivity of the fault mechanical response to the fault criticality and the level of fluid pressurization. Our results imply that faults with low stress state may be initially dominated by aseismic slip, which then promote localized stress transfer and induce earthquakes with low relative stress drop on surrounding branched planes. In contrast, faults that are critically stressed may primarily slip seismically with high relative stress drop. This study highlights the persistence of complex triggering processes of injection-induced earthquakes at very small magnitudes.

References

Abercrombie, R. E. (2015). Investigating uncertainties in empirical Green's function analysis of earthquake source parameters. *Journal of Geophysical Research: Solid Earth*, *120*, 4263–4277. https://doi.org/10.1002/2015JB011984

Bhattacharya, P., & Viesca, R. C. (2019). Fluid-induced aseismic fault slip outpaces pore-fluid migration. *Science*, *364*(6439), 464–468. https://doi.org/10.1126/science.aaw7354

Boore, D. M. (1983). Stochastic simulation of high-frequency ground motions based on seismological models of the radiated spectra. *Bulletin of the Seismological Society of America*, *73*(6), 1865–1894.

Boyd, O. S., McNamara, D. E., Hartzell, S., & Choy, G. (2017). Influence of lithostatic stress on earthquake stress drops in North America. *Bulletin of the Seismological Society of America*, *107*(2), 856–868. https://doi.org/10.1785/0120160219

Brune, J. (1970). Tectonic stress and the spectra of seismic shear waves from earthquakes. *Journal of Geophysical Research*, *75*(26), 4997–5009. https://doi.org/10.1029/JB075i026p04997

Byerlee, J. (1978). Friction of rocks. In *Rock friction and earthquake prediction* (pp. 615–626). Basel: Birkhäuser. https://doi.org/10.1007/978-3-0348-7182-2_4

Cappa, F., Scuderi, M. M., Collettini, C., Guglielmi, Y., & Avouac, J. P. (2019). Stabilization of fault slip by fluid injection in the laboratory and in situ. *Science advances*, *5*(3). https://doi.org/10.1126/sciadv.aau4065

Catalli, F., Rinaldi, A. P., Gischig, V., Nespoli, M., & Wiemer, S. (2016). The importance of earthquake interactions for injection-induced seismicity: Retrospective modeling of the Basel Enhanced Geothermal System. *Geophysical Research Letters*, *43*, 4992–4999. https://doi.org/10.1002/2016GL068932

Daniel, G. (2014). Bias in magnitude for earthquakes with unknown focal mechanism. *Geophysical Prospecting*, *62*(4), 848–861. https://doi.org/10.1111/1365-2478.12142

De Barros, L., Cappa, F., Guglielmi, Y., Duboeuf, L., & Grasso, J. R. (2019). Energy of injection-induced seismicity predicted from in-situ experiments. *Scientific reports*, *9*(1), 4999. https://doi.org/10.1038/s41598-019-41306-x

De Barros, L., Guglielmi, Y., Rivet, D., Cappa, F., & Duboeuf, L. (2018). Seismicity and fault aseismic deformation caused by fluid injection in decametric in-situ experiments. *Comptes Rendus Geoscience*, *350*(8), 464–475. https://doi.org/10.1016/j.crte.2018.08.002

Denolle, M. A., & Shearer, P. M. (2016). New perspectives on self-similarity for shallow thrust earthquakes. *Journal of Geophysical Research: Solid Earth*, *121*, 6533–6565. https://doi.org/10.1002/2016JB013105

Duboeuf, L., De Barros, L., Cappa, F., Guglielmi, Y., Deschamps, A., & Seguy, S. (2017). Aseismic motions drive a sparse seismicity during fluid injections into a fractured zone in a carbonate reservoir. *Journal of Geophysical Research: Solid Earth*, *122*, 8285–8304. https://doi.org/10.1002/2017JB014535

Ellsworth, W. L. (2013). Injection-induced earthquakes. *Science*, *341*(6142). https://doi.org/10.1126/science.1225942

Ellsworth, W. L., & Bulut, F. (2018). Nucleation of the 1999 Izmit earthquake by a triggered cascade of foreshocks. *Nature Geoscience*, *11*(7), 531–535. https://doi.org/10.1038/s41561-018-0145-1

Eshelby, J. D. (1957). The determination of the elastic field of an ellipsoidal inclusion, and related problems. *Proceedings of the Royal Society London A: Mathematical, Physical and Engineering Sciences*, *241*(1226), 376–396. https://doi.org/10.1098/rspa.1957.0133

Goebel, T. H., & Brodsky, E. E. (2018). The spatial footprint of injection wells in a global compilation of induced earthquake sequences. *Science*, *361*(6405), 899–904. https://doi.org/10.1126/science.aat5449

Gomberg, J. (2018). Unsettled earthquake nucleation. *Nature Geoscience*, *11*(7), 463.

Guglielmi, Y., Cappa, F., Avouac, J.-P., Henry, P., & Elsworth, D. (2015). Seismicity triggered by fluid injections induced aseismic slip. *Science*, *348*(6240), 1224–1226. https://doi.org/10.1126/science.aab0476

Guglielmi, Y., Cappa, F., Lancon, H., Janowczyk, J., Rutqvist, J., Tsang, C.-F., & Wang, J. S. Y. (2014). ISRM suggested method for step-rate injection method for fracture in-situ properties (SIMFIP): Using a 3-components borehole deformation sensor. *Rock Mechanics and Rock Engineering*, *47*(1), 303–311. https://doi.org/10.1007/s00603-013-0517-1

Hardebeck, J. L., & Shearer, P. M. (2002). A new method for determining first-motion focal mechanisms. *Bulletin of the Seismological Society of America*, *92*(6), 2264–2276. https://doi.org/10.1785/0120010200

Huang, Y., Beroza, G. C., & Ellsworth, W. L. (2016). Stress drop estimates of potentially induced earthquakes in the Guy-Greenbrier sequence. *Journal of Geophysical Research: Solid Earth*, *121*, 6597–6607. https://doi.org/10.1002/2016JB013067

Huang, Y., Ellsworth, W. L., & Beroza, G. C. (2017). Stress drops of induced and tectonic earthquakes in the central United States are indistinguishable. *Science advances*, *3*(8), e1700772. https://doi.org/10.1126/sciadv.1700772

Ide, S., Beroza, G. C., Prejean, S. G., & Ellsworth, W. L. (2003). Apparent break in earthquake scaling due to path and site effects on deep borehole recordings. *Journal of Geophysical Research*, *108*(B5), 2271. https://doi.org/10.1029/2001JB001617

Imanishi, K., & Ellsworth, W. L. (2006). Source scaling relationships of microearthquakes at Parkfield, CA, determined using the SAFOD pilot hole seismic array. *Earthquakes: Radiated Energy and the Physics of Faulting*, *170*, 81–90.

Jeanne, P., Guglielmi, Y., Lamarche, J., Cappa, F., & Marié, L. (2012). Architectural characteristics and petrophysical properties evolution of a strike-slip fault zone in a fractured porous carbonate reservoir. *Journal of Structural Geology*, *44*, 93–109. https://doi.org/10.1016/j.jsg.2012.08.016

Kaneko, Y., & Shearer, P. M. (2015). Variability of seismic source spectra, estimated stress drop, and radiated energy, derived from cohesive-zone models of symmetrical and asymmetrical circular and elliptical ruptures. *Journal of Geophysical Research: Solid Earth*, *120*, 1053–1079. https://doi.org/10.1002/2014JB011642

Keranen, K. M., & Weingarten, M. (2018). Induced seismicity. *Annual Review of Earth and Planetary Sciences*, *46*(1), 149–174. https://doi.org/10.1146/annurev-earth-082517-010054

Keranen, K. M., Weingarten, M., Abers, G. A., Bekins, B. A., & Ge, S. (2014). Sharp increase in central Oklahoma seismicity since 2008 induced by massive wastewater injection. *Science*, *345*(6195), 448–451. https://doi.org/10.1126/science.1255802

Madariaga, R. (1976). Dynamics of an expanding circular fault. *Bulletin of the Seismological Society of America*, *66*(3), 639–666.

Moos, D., & Zoback, M. D. (1990). Utilization of observations of well bore failure to constrain the orientation and magnitude of crustal stresses: application to continental, Deep Sea Drilling Project, and Ocean Drilling Program boreholes. *Journal of Geophysical Research*, *95*(B6), 9305–9325. https://doi.org/10.1029/JB095iB06p09305

Moré, J. J., & Sorensen, D. C. (1983). Computing a trust region step. *SIAM Journal on Scientific and Statistical Computing*, *4*(3), 553–572. https://doi.org/10.1137/0904038

Raleigh, C. B., Healy, J. H., & Bredehoeft, J. D. (1976). An experiment in earthquake control at Rangely, Colorado. *Science*, *191*(4233), 1230–1237. https://doi.org/10.1126/science.191.4233.1230

Schoenball, M., & Ellsworth, W. L. (2017). Waveform-relocated earthquake catalog for Oklahoma and southern Kansas illuminates the regional fault network. *Seismological Research Letters*, *88*(5), 1252–1258. https://doi.org/10.1785/0220170083

Segall, P., & Lu, S. (2015). Injection-induced seismicity: Poroelastic and earthquake nucleation effects. *Journal of Geophysical Research: Solid Earth*, *120*, 5082–5103. https://doi.org/10.1002/2015JB012060

Sumy, D. F., Cochran, E. S., Keranen, K. M., Wei, M., & Abers, G. A. (2014). Observations of static Coulomb stress triggering of the November 2011 M5. 7 Oklahoma earthquake sequence. *Journal of Geophysical Research: Solid Earth*, *119*, 1904–1923. https://doi.org/10.1002/2013JB010612

Townend, J., & Zoback, M. D. (2000). How faulting keeps the crust strong. *Geology*, *28*(5), 399–402. https://doi.org/10.1130/0091-7613(2000)28<399:HFKTCS>2.0.CO;2

Trugman, D. T., Dougherty, S. L., Cochran, E. S., & Shearer, P. M. (2017). Source spectral properties of small to moderate earthquakes in southern Kansas. *Journal of Geophysical Research: Solid Earth*, *122*, 8021–8034. https://doi.org/10.1002/2017JB014649

Uchide, T., & Imanishi, K. (2016). Small earthquakes deviate from the omega-square model as revealed by multiple spectral ratio analysis. *Bulletin of the Seismological Society of America*, *106*(3), 1357–1363. https://doi.org/10.1785/0120150322

Walsh, F. R., & Zoback, M. D. (2015). Oklahoma's recent earthquakes and saltwater disposal. *Science advances*, *1*(5). https://doi.org/10.1126/sciadv.1500195

Wei, S., Avouac, J. P., Hudnut, K. W., Donnellan, A., Parker, J. W., Graves, R. W., et al. (2015). The 2012 Brawley swarm triggered by injection-induced aseismic slip. *Earth and Planetary Science Letters*, *86*(2A), 344–354. https://doi.org/10.1785/0220140249

Wu, Q., Chapman, M., & Chen, X. (2018). Stress-drop variations of induced earthquakes in Oklahoma. *Bulletin of the Seismological Society of America*, *108*(3A), 1107–1123. https://doi.org/10.1785/0120170335